energies

MDPI

Article

Investigation on Coalbed Methane Fracturing Using Supercritical CO_2 Graphene Cement Slurry System

Dongyuan Li [1], Pingya Luo [1,*], Xiaojun Peng [2], Tao Zou [3], Li Fu [1], Wanchun Fu [4] and Gang Xie [1,*]

[1] State Key Laboratory of Oil & Gas Reservoir Geology and Exploitation, Southwest Petroleum University, Chengdu 610500, China
[2] Wuhuan Engineering Co., Ltd., Wuhan 430223, China
[3] Huabei Oilfield Company, China National Petroleum Corporation, Renqiu 062552, China
[4] Chengdu GSUN Energy Technology Co., Ltd., Chengdu 610219, China
* Correspondence: luopy@swpu.edu.cn (P.L.); 201899010129@swpu.edu.cn (G.X.)

Abstract: In this study, we innovatively use sulphoaluminate cement slurry and its additives as a fracturing fluid system for supercritical CO_2 graphene-permeable cement stone (referred to hereafter as the SCGPCS) fracturing without sand. Utilizing small fluid volumes, small displacement and small pump pressure, we obtain the success of the first field test in an extra-low desorption pressure coal seam. Laboratory experiments have proven that sulphoaluminate cement is suitable as base cements for the SCGPCS system due to their rapid setting and fast hardening characteristics. The reaction of sodium carbonate + aluminum sulfate system and sodium bicarbonate + aluminum sulfate system will generate precipitation to block the internal pore structure of cement stone, leading to a decrease in permeability. Calcium hypochlorite (1.5 wt.%) + urea (0.6 wt.%) system is preferred as a gas-generating agent system for SCGPCS. Sand (30 wt.%) with 300–425 μm particle size is preferred as a structural strength substance for SCGPCS. Graphene poly-gel (referred to hereafter as the GPG) has a high FCI and good CO_2 foam stability. GPG (6.0 wt.%) is preferred as a foam stabilizer for SCGPCS. The thickening time of graphene–foam–cement slurry is 138 min at 50 °C, with long pumping time, normal thickening curve and excellent performance. The SCGPCS has a corrosion rate of 11.25 mpy in the formation water and can be stable in the formation. Acid is more corrosive to SCGPCS, and it can be used to improve the permeability of SCGPCS. Field tests have proven that SCGPCS fracturing injected 33 m^3 of fluid, of which 27 m^3 entered the formation. Graphene–foam–cement slurry was injected into the formation through the casing for 13 m^3, with a displacement of 0.4–0.6 m^3/min and tubing pressure 8–13 MPa. The formation was fractured with a fracturing crack half-length of 71.58 m, a supported fracturing crack half-length of 56.95 m, and a supported fracturing crack permeability of 56.265 mD.

Keywords: supercritical CO_2; permeable cement stone; sulphoaluminate cement; graphene poly-gel; permeability; compressive strength; coalbed methane fracturing

Citation: Li, D.; Luo, P.; Peng, X.; Zou, T.; Fu, L.; Fu, W.; Xie, G. Investigation on Coalbed Methane Fracturing Using Supercritical CO_2 Graphene Cement Slurry System. *Energies* **2022**, *15*, 7624. https://doi.org/10.3390/en15207624

Academic Editor: Mofazzal Hossain

Received: 18 September 2022
Accepted: 12 October 2022
Published: 15 October 2022

1. Introduction

Methane emission reduction and CO_2 storage are now key points in the global net-zero emissions [1]. The development of coalbed methane and gas hydrate using CO_2 replacement enables both CO_2 storage and efficient exploitation of methane [2,3].

Coal seams are generally characterized by low pressure, low permeability and strong non-homogeneity [4–6]. In order to make coalbed methane development reach industrial exploitation, production stimulation measures are necessary. Hydraulic fracturing is the preferred method and the main measure to increase production in coalbed methane wells [7–11]. After hydraulic fracturing, the coal seam fractures are pressed open and proppant is added to form multiple seepage zones with high inflow capacity, effectively connecting the wellbore and the reservoir, which can achieve the purpose of promoting drainage and increasing the rate of gas production [12,13].

Coal-bearing strata have experienced strong tectonic movements after coal formation, and the original structure of coal seams has been destroyed and plasticity enhanced [14,15]. Coalbed methane fracturing faces a series of technical difficulties, resulting in a poor fracturing effect at the initial stage, which in turn leads to short continuous production time and low gas production at the later stage [16–18]. By studying the characteristics of coalbed methane reservoirs and summarizing the on-site fracturing construction experience, it is believed that the main reasons for the low efficiency of coalbed methane development are as follows. Large plasticity of coal seam. The coal seam mainly undergoes plastic deformation during hydraulic fracturing, which cannot further extend the natural fractures and cuttings, resulting in the inability to form a large number of long fractures for effective hydraulic fracturing. The difference between the hardness of the proppant and the hardness of the coal seam is large, and the embeddedness of the proppant leads to the inability to achieve effective support for a long time, and the fractures are easy to close [19–21]. Natural fractures exist in the coal seam. Fracturing can easily cause serious filtration loss, which causes coal matrix swelling and pore blockage and affects the permeability of the coal seam [22,23]. The coal rock has low Young's modulus and large Pine ratio. Coal fines are easy to produced to block the original coalbed methane seepage channels and affect the production of coalbed methane [24–26].

Instead of pumping proppants into the well, a revolutionary way is investigated to generate the proppants in the fracturing cracks [27,28]. The new fracturing fluid is solids free. When the fracturing fluid is extruded into the fracture, it is solidified under the temperature conditions of the formation, forming spherical proppant particles with certain compressive strength. The chemistry can be tuned to generate proppant with different particle sizes under different temperature. But the stiffness of the situ forming proppant is very low, and it is difficult to apply in fracturing sites. The chemistry is susceptible to the influence of other materials in the formation during consolidation. This study designs and optimizes a graphene–CO_2 foam–cement slurry system adapted to coalbed methane fracturing. Compared with conventional hydraulic fracturing, the inorganic gel system is creatively used as an in situ forming proppant for coalbed methane fracturing. The graphene–CO_2 foam–cement slurry is injected into the coal seam fracture at high pressure and solidified to form a supercritical CO_2 graphene permeable cement stone (SCGPCS) with certain compressive strength, which will form multiple high-infiltration fractures under the pressure of the overlying rock layer. Graphene–foam–cement slurry with small liquid volume, small displacement and low pumping pressure solves the problem of coal fines generation and migration during fracturing. SCGPCS solves the problem of proppant embeddedness and backflow with full filling in the cracks. SCGPCS reinforced coal seams and high permeability, solving the problems of short continuous production time and low gas production in the late stage of coalbed methane production.

2. Materials and Methods

2.1. Materials

Sulphoaluminate cement was obtained from Jiahua Special Cement Co., Ltd., Leshan, China. Sand was provided by Chengde Beiyan New Material Technology Co., Ltd., Chengde, China. Calcium hypochlorite, urea, aluminum sulfate, sodium carbonate and sodium bicarbonate were purchased from Chengdu Kelong Chemical Co., Ltd., Chengdu, China. A dispersant and water-reducing agent was obtained from Tianjin Kelioil Engineering Material and Technology Co., Ltd., Tianjin, China. Calcium Stearate was purchased from Nanjing Steamboat Chemical Co., Ltd., Nanjing, China. Sodium carboxymethyl cellulose was purchased from Qingdao Urso Chemical Technology Co., Ltd., Qingdao, China. Lignosulfonate was purchased from Jinan Xinlong Chemical Co., Ltd., Jinan, China. GPG was synthesized by laboratory. All chemicals are chemically pure.

2.2. Preparation of SCGPCS

The prepared additives were added to the sulphoaluminate cement in mass ratio, stirred with a glass rod and set aside; a quantity of water was added to a 1200 mL steel cup in mass ratio and set aside; the high-speed mixer was switched on and the mixing rate was set at 4000 r/min; the cement was poured into the steel cup, stirred for approximately 20 s and then poured into the mold. The prepared cement slurry molds were placed in a repellent intermediate vessel, pressurized to 10 MPa, the temperature was raised to 40 °C and it was cured for 72 h; the SCGPCS was cured and processed into standard cores (25 mm × 50 mm); the cores were dried at 60 °C for 60 h and set aside. Figure 1 shows the prepared SCGPCS.

(**a**) (**b**)

Figure 1. The Core column of SCGPCS. (**a**) Longitudinal section. (**b**) Cross-section.

2.3. Preparation of GPG

Graphene nanosheets, double-soluble surfactants and nonionic surfactants were added to ethanol or propanol volatile environment-friendly dispersant with boiling point below 100 °C in certain proportions, stirred and mixed well to make graphene dispersion; a graphene dispersion substance was put into a non-metallic closed container and heated by microwave; volatile dispersant was completely evaporated and vaporized at 90–100 °C, and surfactants around graphene nanosheets form highly dispersed concentrated laminate foam; graphene laminate foam was released to atmospheric pressure by ultrasonic vibration, cooled to room temperature, and finally coalesced into graphene concentrated poly-gel. Figure 2 shows the prepared GPG.

Figure 2. GPG prepared.

2.4. Test Methods

2.4.1. Testing of Permeability of SCGPCS

The standard core of SCGPCS was put into a phase permeability tester (XSY-3, Haian Petroleum Research Instruments Co., Ltd., Nantong, China) for water and gas permeability testing, and the average value was taken and accurate to 0.1 mD. The test circumferential pressure was 2.50 MPa, the displacement pressure was 0.20–0.30 MPa, and the test time was 30 min. The permeability is calculated by Darcy's law:

$$K = 10^5 \times \frac{Q \times \mu \times L}{A \times \Delta P} \quad (1)$$

K—Permeability, D;
Q—Flux, mL/s;
μ—Viscosity of fluid, Pa·s;
L—Sample length, cm;
A—Sample cross-sectional area, cm^3;
ΔP—Differential pressure, kPa.

2.4.2. Testing of Compressive Strength of SCGPCS

The standard core of SCGPCS was placed in the center of the support block of the automatic cement pressure tester (YAW-300, Jinan Kanyuan Testing Instruments Co., Ltd., Jinan, China), and the load was applied to the surface in contact with the plane of the test block for compressive strength testing. Three parallel samples were taken at the same time, and the average value was taken and accurate to 0.1 MPa as the test result of compressive strength.

2.4.3. Testing of Cement Slurry Thickening Curve

The mixed cement slurry was poured into the slurry cup. The slurry cup was placed into the an atmospheric consistometer (HTD125, Qingdao Haitongda Special Instrument Co., Ltd., Qingdao, China), which recorded the temperature, pressure, consistency curve, and experimental data in real time. This could be output from an external data interface to an external computer, where the computer screen displayed the experimental curve while the test results were finally printed out by a color printer. An atmospheric consistometer can automatically control the rate of temperature rise (temperature gradient) and maintain a constant temperature when the cement slurry reaches the set temperature with an accuracy of <1 °C (33.8 °F). At the same time, it can automatically control the rate of pressure rise (pressure gradient) and the pressure in the kettle is provided by a pneumatic ultra-high-pressure pump and maintained by a pneumatic control valve.

2.4.4. Testing of Foam Stabilizer Performance

The prepared solution 150 mL was added to a 250 mL beaker and placed in a six-speed rotating viscometer to test the apparent viscosity of the corresponding solution. After the test, the solution was poured into a Warring mixer and the foam stabilizer was added to the solution in proportion to the volume. CO_2 gas was introduced into the mixing cup and stirred at 2000 rpm for 2 min. The foam generated was poured into a measuring cylinder to record the volume of foam generated and the mouth of the cylinder was covered with a double layer of plastic wrap. The cylinder was placed in an oven at a pre-set temperature to test the half-life of the corresponding foam.

Foam Composite Index (referred to hereafter as the FCI):

$$FCI = V_0 \times t_{1/2} \quad (2)$$

V_0—Initial foaming volume, mL;
$t_{1/2}$—Half-life, min.

2.4.5. Testing of XRD, SEM and Microscope

The phase composition of the samples was analyzed with an X-ray diffractometer (X'Pert MPD PRO, Paneth, Holland) under Cu (Kα) radiation (V = 40 kV, I = 40 mA) at a scanning speed of 2°/min in the range of 5–70°. The sample to be measured was scattered on a conductive tape, and the conductive tape was attached to a stainless-steel plate. Due to the non-conductive nature of the sample, a thin layer of gold was sprayed onto the surface of the test sample. The morphology of the samples was observed with a scanning electron microscope (SEM) (Quanta 450, FEI Co., Hillsboro, OR, USA) at 20.00 kV. The pore structure of the samples was tested with an electron microscope (CMM-50, Shanghai Changfang Optical Instruments Co., Ltd., Shanghai, China).

3. Results and Discussion

3.1. Optimization of Cement Slurry System

3.1.1. Selection of Cement Types

The SCGPCS system uses sulphoaluminate cement, which can set quickly after entering the formation and reach a large strength in a short period of time, able to form an effective fracture support structure after fracturing. Oil well G-grade cement takes a long time to reach a certain strength after setting. After the fracturing fractures are closed, the set cementite is less strong and easier to crush. More cement debris and particles are produced, blocking the fluid channels established by the cement itself, which has a greater negative impact on coalbed methane production.

3.1.2. Preferred Gas-Generating Agent System

Gas-generating agent can be used in a calcium hypochlorite + urea system, sodium carbonate + aluminum sulfate system, sodium bicarbonate + aluminum sulfate system. The reaction equations are shown in Equations (2)–(4); these three reactions are exothermic reaction.

$$3Ca(ClO)_2 + 2CO(NH_2)_2 \rightarrow 2N_2 \uparrow + 2CO_2 \uparrow + 3CaCl_2 + 4H_2O \quad (3)$$

$$3Na_2CO_3 + Al_2(SO_4)_3 + 3H_2O \rightarrow 3CO_2 \uparrow + 3Na_2SO_4 + 2Al(OH)_3 \downarrow \quad (4)$$

$$6NaHCO_3 + Al_2(SO_4)_3 \rightarrow 6CO_2 \uparrow + 3Na_2SO_4 + 2Al(OH)_3 \downarrow \quad (5)$$

The reaction of aluminum sulfate + sodium carbonate system and aluminum sulfate + sodium bicarbonate system will generate gas and precipitate. The microporous structure of cement stone is easily blocked by precipitation, which causes more harm to permeability. The reaction of calcium hypochlorite + urea system only produces gas and soluble ionic compounds, which will not harm the permeability of cement stone. It is a more ideal gas-generating agent system.

Figure 3 indicates that the calcium hypochlorite + urea gas-generating system produces the largest volume of total gas. This is because the system not only produces CO_2 but also N_2. The sodium carbonate + aluminum sulfate gas-generating system produces the largest volume of CO_2. The sodium bicarbonate + aluminum sulfate gas-generating system produces the smallest volume of gas.

1. Effect of different concentrations of a calcium hypochlorite + urea gas-generating system on the performance of cement stone.

Figure 4 shows that the volume of gas generated inside the cement stone increases with the increase in calcium hypochlorite mass concentration. The increase in pore space inside the cement stone core leads to the increase in permeability. When the mass concentration of calcium hypochlorite is greater than 1.5%, the permeability of the cement stone core increases, while the compressive strength decreases. This is because the larger the internal pore space of cement stone under a certain pressure, the more easily the space structure is destroyed, and the compressive strength will be reduced [29,30].

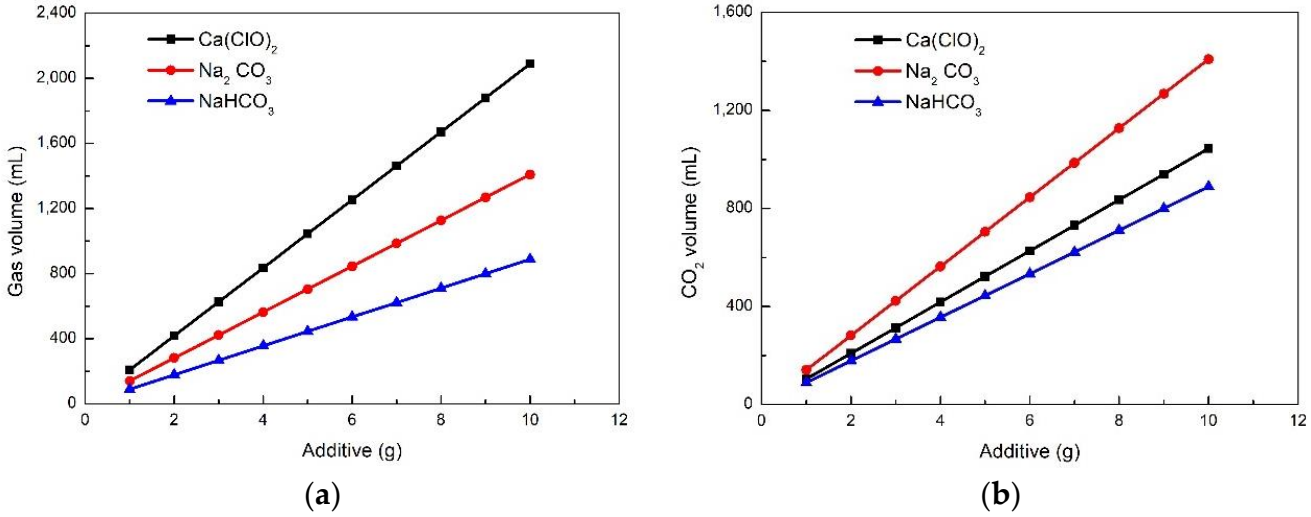

Figure 3. Effect of gas-generating agent addition on the volume of generated gas. (**a**) Gas volume. (**b**) CO_2 volume.

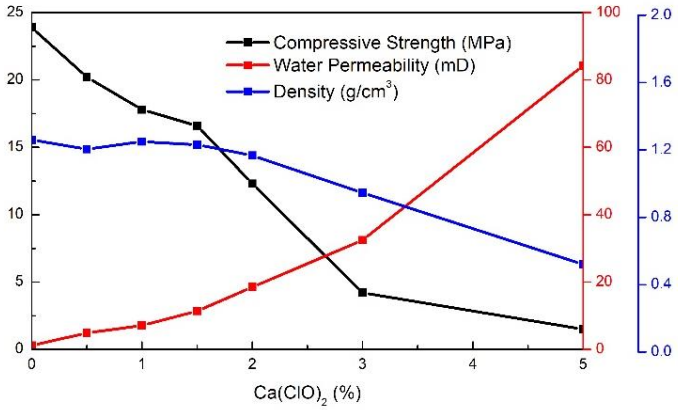

Figure 4. Effect of different mass concentrations of calcium hypochlorite + urea gas-generating system on the performance of cement stone.

2. Effect of different concentrations of sodium carbonate + aluminum sulfate gas-generating system on the performance of cement stone.

Figure 5 shows that the permeability of cement stone core increases with the increase in sodium carbonate mass concentration, while the compressive strength decreases. The permeability of sodium carbonate + aluminum sulfate gas-generating system is smaller than that of calcium hypochlorite + urea gas-generating system under the same amount of addition. The reason is that calcium hypochlorite + urea gas-generating system generates large volumes of gas. At the same time, a sodium carbonate + aluminum sulfate gas-generating system generates gas and precipitation, and the precipitation will block the pore structure of the cement stone, resulting in a decrease in permeability.

3. Effect of different concentrations of sodium bicarbonate + aluminum sulfate gas-generating system on the performance of cement stone.

Figure 6 illustrates that the volume of gas generated increases with the increase in the mass concentration of sodium bicarbonate, resulting in an increase in the permeability of the cement stone. When the mass concentration of sodium bicarbonate in the cement slurry is greater than 0.5%, the precipitation generated by the reaction blocks the microscopic pores inside the cement stone, resulting in a decrease in permeability. When the mass concentration of sodium bicarbonate continues to increase, the effect of the generated gas on the increase in cement stone permeability is enhanced, and the effect of precipitation on the decrease in cement stone permeability is weakened.

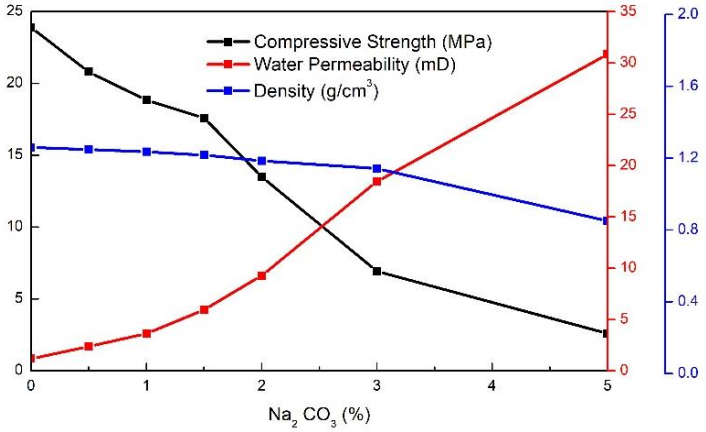

Figure 5. Effect of different mass concentrations of sodium carbonate + aluminum sulfate gas-generating system on the performance of cement stone.

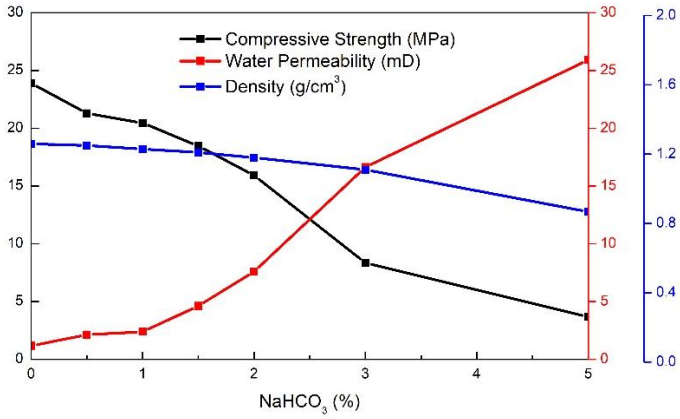

Figure 6. Effect of different mass concentrations of sodium bicarbonate + aluminum sulfate gas-generating system on the performance of cement stone.

The experiments proved that the cement stone prepared by the calcium hypochlorite + urea gas-generating system has good permeability. The reaction of sodium carbonate + aluminum sulfate gas-generating system and sodium bicarbonate + aluminum sulfate gas-generating system will generate precipitation to block the internal pore structure of cement stone, leading to a decrease in permeability. The calcium hypochlorite + urea gas-generating system was selected as the gas-generating agent for permeable cement stone, with the optimum concentration of 1.5%.

3.1.3. Effect of Sand on the Performance of Cement Stone

Figure 7 indicates that the permeability of permeable cement stone increases first and then decreases with the increase in sand particle size. The permeability of permeable cement stone core is greatest when the quartz sand particle size is 300–425 μm. The quantity of sand of the same quality decreases with the increase in sand particle size, which reduces the accumulation between sands. The permeable cement stone consolidated more tightly, and the permeability decreases, while the compressive strength of permeable cement stone increases. Sand with particle size 300–425 μm is selected as the permeable cement stone structuring strength substance.

Figure 8 shows that the permeability of permeable cement stone increases with the increase in sand mass concentration, and at the same time the compressive strength decreases. The increase in the amount of sand increases the volume of accumulation between the particles. It makes the porosity inside the cement stone increase and improves the permeability of the cement stone. The optimum mass concentration of sand is 30%.

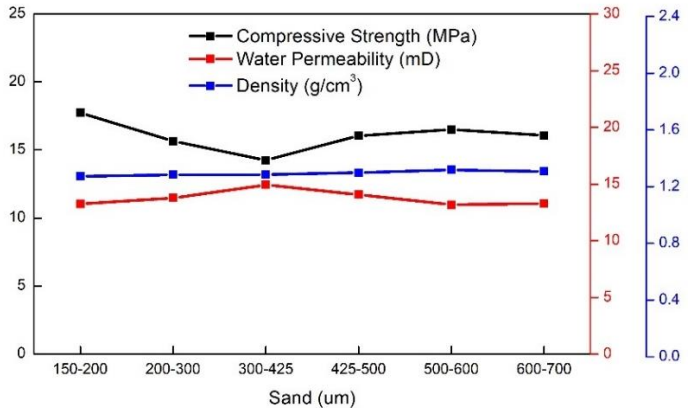

Figure 7. Effect of different particle sizes of sand on the performance of permeable cement stone.

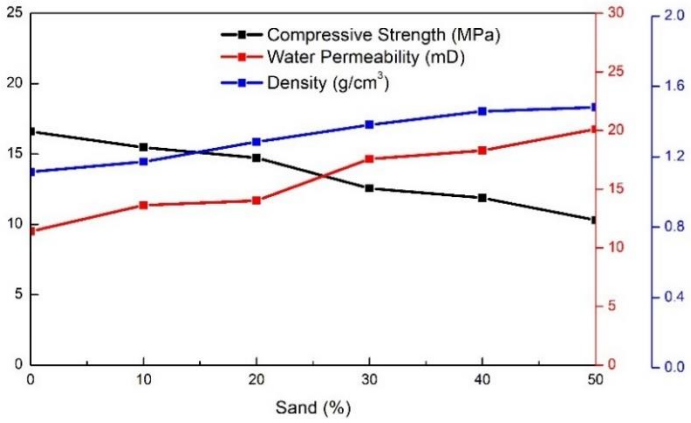

Figure 8. Effect of different mass concentrations on the performance of permeable cement stone.

3.2. Graphene Poly-Gel (GPG) System

3.2.1. Structure of GPG

Figure 9 shows that GPG consists of graphene nanosheet cores, hydrophilic and oleophilic lamination and surfactant micelles. GPG has unique properties such as high specific surface area, high dispersion, high levels of foam and high thermal conductivity. It can be used as foam stabilizer for the foam–cement slurry system.

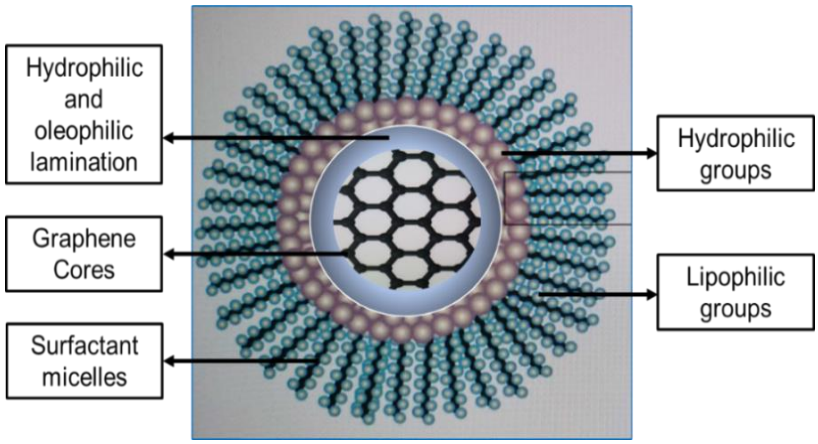

Figure 9. The Structure of GPG.

3.2.2. Effect of Different Temperatures on the Performance of Foam Stabilizers

The effects of foaming volume, half-life and FCI of calcium stearate, sodium carboxymethyl cellulose, lignin sulfonate and GPG at different temperatures were compared, as shown in Figure 10.

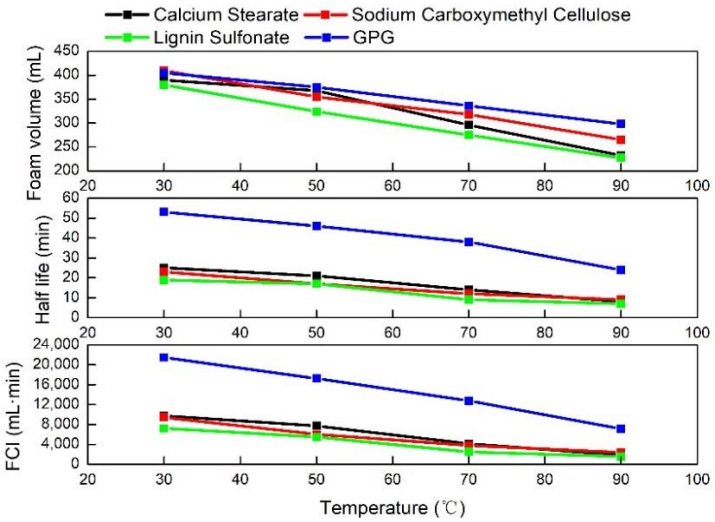

Figure 10. Effect of different temperatures on the performance of foam stabilizers.

Figure 10 illustrates that the initial foam volume and half-life time of all four foam stabilizers decreased as the temperature increased. This shows that high temperature will inhibit the foam stabilization performance of the foam stabilizer. The reasons for this analysis are as follows.

1. The surface viscosity of the foam decreases as the temperature rises and the foam stability decreases. The key factor to determine the stability of the foam is the strength of the liquid film. The strength of the liquid film mainly depends on the robustness of the adsorption film on the surface, and the surface viscosity is used as a quantitative indicator of the robustness of the adsorption film in the data. The higher the surface viscosity, the stronger the foam stability. It is mainly determined by three mechanisms: large surface viscosity increases the surface strength of the liquid film; large surface viscosity makes the liquid on the surface of the liquid film not easy to flow, and the drainage effect is weakened; large surface viscosity makes the gas inside the foam not easy to diffuse outward through the liquid film. It can be considered that increasing the surface viscosity is the key to increase the stability of the foam. Therefore, when the temperature increases, the foam surface viscosity decreases, resulting in a rapid weakening of foam stability.

2. The higher the temperature, the more violent the charge movement on the foam surface, resulting in a more unstable foam. When the foam–cement slurry enters formation, it will contact a large amount of formation water. The mineralization of the formation water is tens or even hundreds of times higher than that of the surface water, so there are a lot of electrolytes in the foam system. When the temperature rises, the irregular movement of these electrolytes in the foam film becomes more and more violent, which accelerates the draining effect on the foam surface and makes the foam film thinner until it breaks.

The core of GPG is graphene nanosheets. First, the nanoparticles (with solid particle characteristics) can adsorb on the gas–liquid interface to form a liquid film with high mechanical strength and enhance the stability of the foam. The particles are difficult to desorb from the liquid film and will move together with the liquid film. The network structure formed by the interaction force between nanoparticles greatly increases the energy potential barrier, which weakens the liquid film discharge and reduces the aggregation rate of bubbles, thus playing an important protective role in foam stability. Secondly, graphene nanosheets have good thermal conductivity, which can conduct heat from the foam surface

to reduce the temperature of the foam surface, thus achieving the effect of stabilizing the foam. Although the foaming volume and half-life of GPG also decrease with the increase in temperature, the foam instability caused by high temperature is mitigated by the high thermal conductivity of graphene nanosheets [31]. GPG has the highest FCI and the best foam stabilization effect.

3.2.3. Graphene–Foam–Cement Slurry Hydration Exothermic Self-Lifting Temperature and Pressure

Figure 11 shows that the change curve of internal temperature and pressure of graphene–foam–cement slurry during hydration. The internal temperature of graphene–foam–cement slurry was maintained at about 20 °C until 20 min. The hydration reaction started to exotherm and the internal temperature of graphene–foam–cement slurry started to increase after 20 min. The internal temperature of cement stone reached 69 °C at 42 min and was maintained at this temperature. The internal pressure of graphene–foam–cement slurry is also changing with time. The pressure is 0 MPa at the beginning of hydration, reaches a small peak of 10 MPa at 14 min, and then drops back to 7 MPa. The pressure continues to increase with time after 27 min and reaches 23 MPa at 120 min. The CO_2 generated inside the graphene–foam–cement slurry is in a supercritical state after 25 min, when the temperature exceeds 31 °C and the pressure exceeds 7.3 MPa.

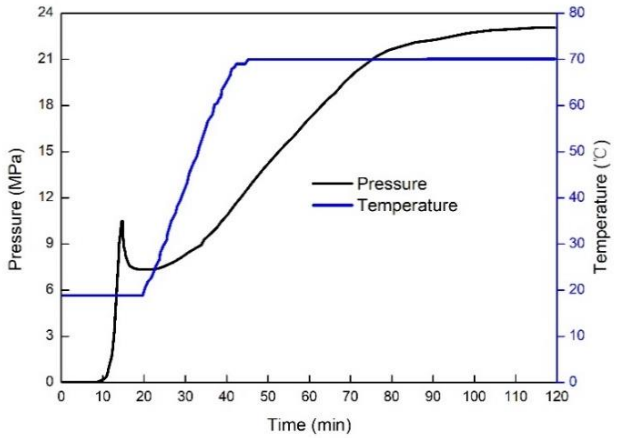

Figure 11. The curve of exothermic internal temperature and pressure during hydration of graphene–foam–cement slurry.

The hydration of cement causes the internal temperature of cement stone to be too high, even over 70 °C. The stabilizing performance of the foam stabilizer will decrease under high-temperature conditions, leading to the rupture of the bubbles generated inside the cement stone, which cannot exist stably. The ruptured bubbles cannot form effective pores inside the cement stone, resulting in the reduction of cement stone porosity. Graphene in GPG has good thermal conductivity. The heat generated by the hydration of cement can be quickly conducted out through the graphene on the surface of the foam, reducing the temperature inside the cement stone and enabling the foam to exist stably. The graphene in GPG enables better dispersion of the generated foam and finer foam formation, and also conducts the heat of cement hydration more and faster with its own high thermal conductivity to ensure the stability of the foam generated inside the cement stone.

Figure 12 illustrates that the graphene is uniformly distributed within the liquid film on the foam surface. Graphene nanosheets are adsorbed into the liquid film of the foam to improve the strength of the liquid film and enhance the stability of the foam. The interaction between the graphene nanosheets adsorbed into the liquid film forms a spatial network structure, which reduces the liquid film drainage and bubble aggregation rate, and enhances the foam stability [32,33]. The high dispersion of graphene nanosheets forms

uniformly dispersed nanofoam. The graphene nanosheets gathered on the surface of the foam can conduct the heat out of the foam quickly.

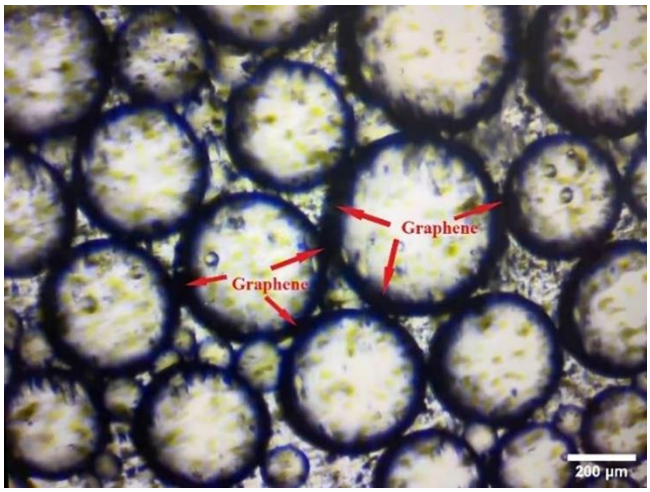

Figure 12. Microstructure of GPG foam under electron microscope.

3.3. Effect of GPG on the Performance of Permeable Cement Stone

Figure 13 shows that the gas permeability and water permeability increased with the increase in GPG mass concentration. The maximum gas permeability reached 154.3 mD and the water permeability reached 90.65 mD. The addition of GPG increased the bubble stabilization ability of CO_2 bubbles, which made the bubble dispersion more uniform and stable. The graphene–foam–cement slurry formed a more stable porous material after consolidation, which improved the permeability. The compressive strength decreased with the increase in GPG mass concentration. More pore structure will reduce the structural strength of cementite, resulting in a decrease in compressive strength. The optimum mass concentration of GPG is 6%. The water permeability of permeable cement stone is 57.24 mD, and the compressive strength of permeable cement stone is 10.19 MPa.

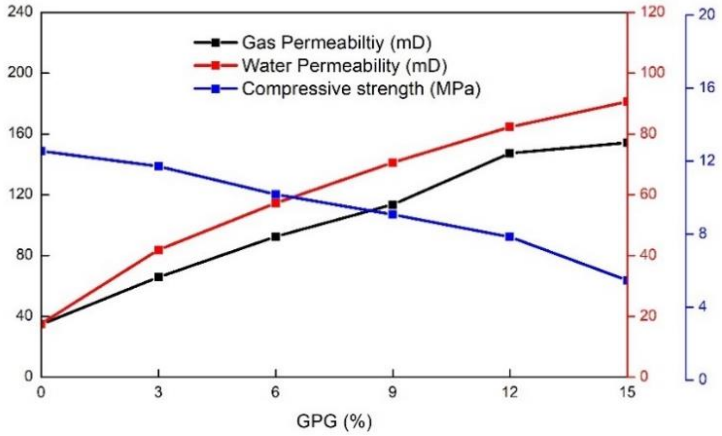

Figure 13. Effect of GPG on the performance of permeable cement stone.

Figure 14a shows that the pores formed after hydration and consolidation of permeable cement stone without GPG have smaller pore size, less number and farther distance from each other, and are not easy to connected. Because there is no foam stabilizer, the CO_2 and N_2 foam generated by the gas-generating agent system struggles to exist stably in the environment of exothermic heating of cement hydration. On the one hand, the foam surface viscosity decreases with the increase in temperature, and the foam liquid film surface strength also decreases, which makes the foam easy to break. On the other hand,

the charge movement on the foam surface becomes more and more violent with the increase in temperature, and the foam becomes more and more unstable until it breaks.

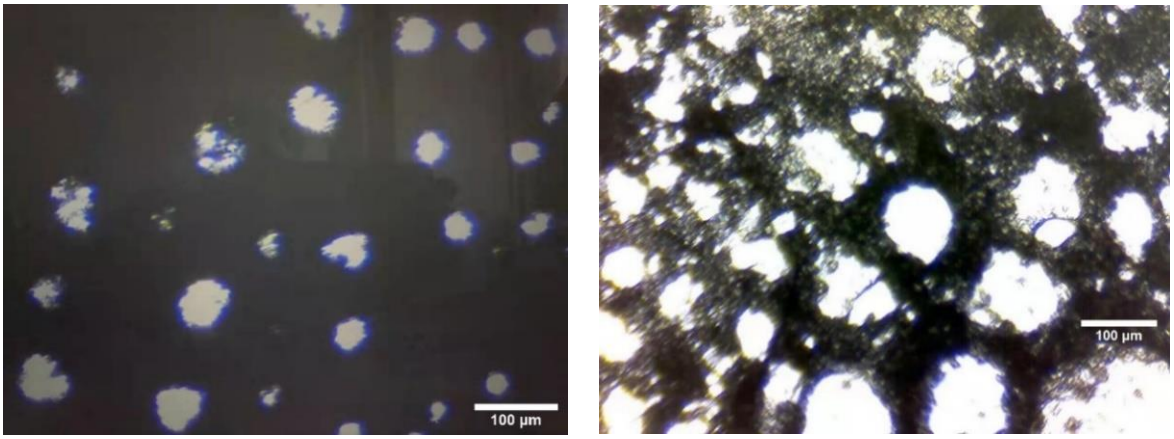

(**a**) (**b**)

Figure 14. Electron micrographs of the pore structure of permeable cement stone (cross-section). (**a**) Without GPG. (**b**) Add 6% GPG.

Figure 14b shows that the pores formed by the hydration consolidation of permeable cement stone with 6% GPG are large, numerous, staggered and well connected. The surfactant in GPG makes it easy for the gas-generating agent system to generate bubbles, and more and more bubbles will be generated under the shearing action of the formation pore throat. However, more heat is released with the hydration reaction of the graphene–foam–cement slurry, resulting in a rapid increase in the internal temperature of the graphene–foam–cement slurry. The highly dispersed graphene in GPG will be distributed on the surface of the liquid film of the foam to improve the strength of the liquid film. At the same time, graphene will use its high thermal conductivity to transfer the heat inside the cement stone to the outside of the cement stone quickly, reducing the temperature inside the cement stone and ensuring the stability of the generated foam.

3.4. Temperature Rise and Pressure Drop to Improve Permeability of SCGPCS

The graphene–foam–cement slurry is pumped into the coal seam fracture at high pressure, and the pressure will diffuse into the formation after the pump is stopped. The pressure generated in the process of hydration of graphene–foam–cement slurry will also diffuse into the formation, creating a pressure drop. The exothermic hydration of the graphene–foam–cement slurry generates a large amount of heat, resulting in an increase in the internal temperature of the graphene–foam–cement slurry. Figure 15a presents that the temperature rise and pressure drop inside the graphene–foam–cement slurry will cause the supercritical CO_2 bubbles to become larger. The increase in external pressure causes the deformation of the enlarged bubbles, which makes the walls of the bubbles inside the cement paste thinner. The increase in bubble volume can form a larger pore structure and improve the porosity of cement stone after consolidation. Figure 15b illustrates that CO_2 within the pore dissolves in the water within the cement stone at the formation temperature and pressure, forming a carbonic acid solution. The carbonic acid solution is corrosive at the formation temperature and dissolves some of the material in the cement stone, which connects the formed pore structure and improves the permeability of the cement stone.

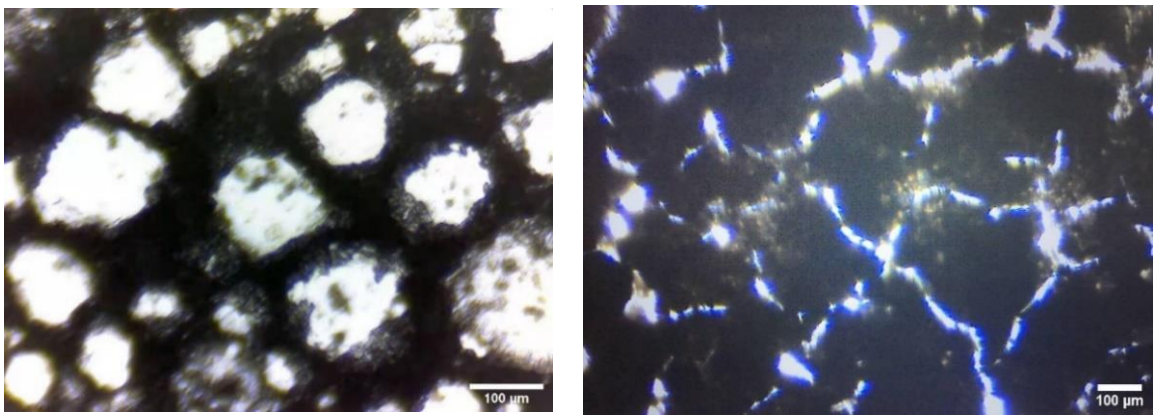

(**a**) (**b**)

Figure 15. Microscopic pores of SCGPCS. (**a**) Cross-section. (**b**) Longitudinal section.

3.5. Compressive Strength of SCGPCS

The SCGPCS was cured at 50 °C. Figure 16a shows that only the characteristic diffraction peaks of ettringite (AFt) and aluminum hydroxide (AH3) appear in the hydration products [34,35]. The sharp peaks and narrow peak widths of the hydration products indicate the high crystallinity of AFt and AH3. The intensity of the diffraction peaks of AFt and AH3 increased with the increase in the curing temperature, indicating that the content of AFt and AH3 in the hydration products increased. The increase in temperature is favorable to the hydration reaction [36–38]. Figure 16b indicates that a large amount of needle-like AFt appears at the curing temperature of 50 °C. The main chemical composition of sulphoaluminate cement is tricalcium aluminate, and the hydration products are mainly AFt and AH3. The hydration reaction of sulphoaluminate cement is rapid, and a large amount of needle-like AFt and AH3 with high strength is produced at the initial stage [39–42]. AFt with high strength ensures that the SCGPCS has a certain compressive strength.

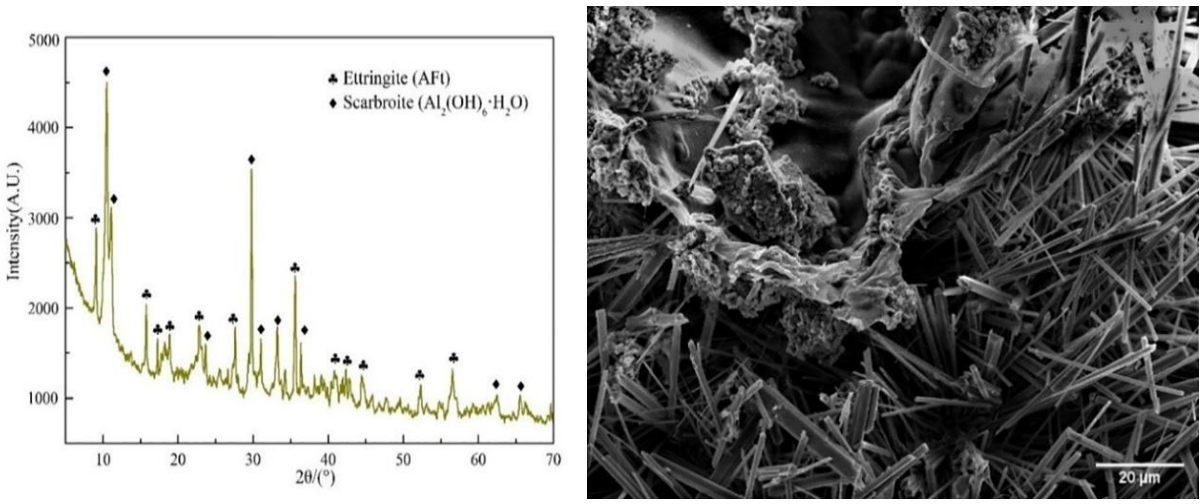

(**a**) (**b**)

Figure 16. Micrograph of compressive strength of SCGPCS. (**a**) XRD diagram. (**b**) SEM.

3.6. Rheology of Graphene–Foam–Cement Slurry System

Figure 17 presents that the initial consistency of the graphene–foam–cement slurry system is 12 Bc, and the thickening time is 138 min, with a long pumping time. The fluidity of the system is 25.50 cm, and the API water loss at 50 °C/6.9 MPa is 58 mL. The thickening curve is normal, there are no abnormal gelling phenomena such as "bulging"

and "stepping", and the performance is excellent. The graphene–foam–cement slurry system ensures safe and smooth fracturing operations.

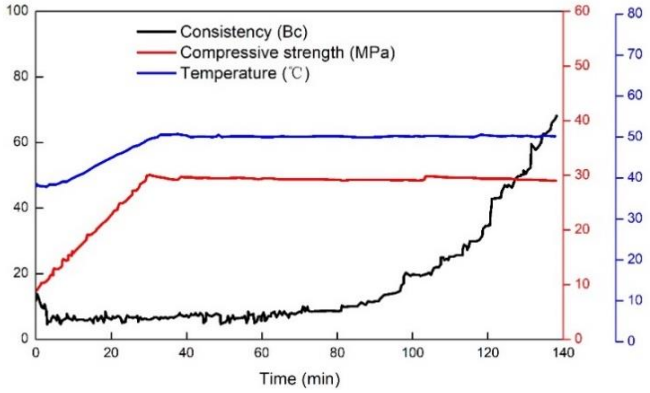

Figure 17. Graphene–foam–cement slurry system thickening curve.

3.7. Experimental Study on Medium Erosion Resistance of SCGPCS

Figure 18 indicates the corrosion rates of SCGPCS in different erosive media. The four media are fresh water, formation water, 1% NaOH solution and 1% HCl solution. The SCGPCS has a certain corrosion rate in fresh water and formation water, which indicates that there are certain substances inside the SCGPCS dissolved in fresh water and formation water. The fresh water and formation water will cause some erosion of the hydration products of SCGPCS, but the effect is not significant. SCGPCS will maintain the stability of its performance in this environment for a long time. When the SCGPCS is immersed in 1% NaOH solution, the corrosion rate is almost negligible, indicating that the alkali solution has no effect on the SCGPCS. When the SCGPCS is immersed in 1% HCl solution, the corrosion rate is large. This is because H^+ invades into the cement stone and dissolves a large amount of cemented material, even destroying the structure of hydration products, which will lead to an increase in permeability and a decrease in compressive strength [43,44]. If the gas production does not reach the expectation after fracturing, the SCGPCS in the formation can be acidified with dilute HCl solution to increase its permeability.

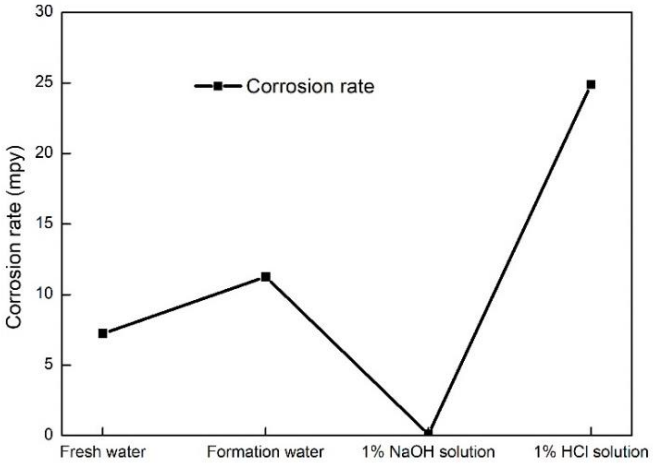

Figure 18. Corrosion rate of SCGPCS under the action of different erosive media.

4. Field Test of SCGPCS Fracturing

4.1. Introduction of Well Conditions

The coal reservoir is a low-porosity and low-permeability reservoir, and the coal structure is primary-fractured coal, brittle and fragile. The cuttings of the coal seam are developed and dense, but with poor continuity and no filler, which is favorable for

fracturing operation. It is planned to explore the adaptability of permeable cement stone fracturing technology in coalbed methane development through permeable cement stone fracturing field tests, and to prepare the technical reserve for the overall development of the block.

4.2. Operation Design

Based on the physical characteristics of coal structure as primary-fractured coal and cuttings development, the SCGPCS system was used for coalbed methane fracturing to achieve the stimulated reservoir volume (SRV) of coal seam. In the first step, the coal seam-cleaning fluid was injected into the pores and natural fractures of the coal seam to dissolve water-insoluble inorganic and organic materials, clear the pore throat and increase the permeability. In the second step, graphene–foam–cement slurry was injected into the coal seam at high pressure to open the end cuttings and face cuttings. A three-dimensional microfracture network with ultra-thin and super-large surface was formed. Nano CO_2 foam, graphene aerogel and high permeability cement stone support the microfracture network. At last, coalbed methane was desorbed from the support fracture surface through self-generated thermal desorption and self-generated CO_2 replacement of SCGPCS. Figure 19 shows the flow chart of On-site fracturing operation.

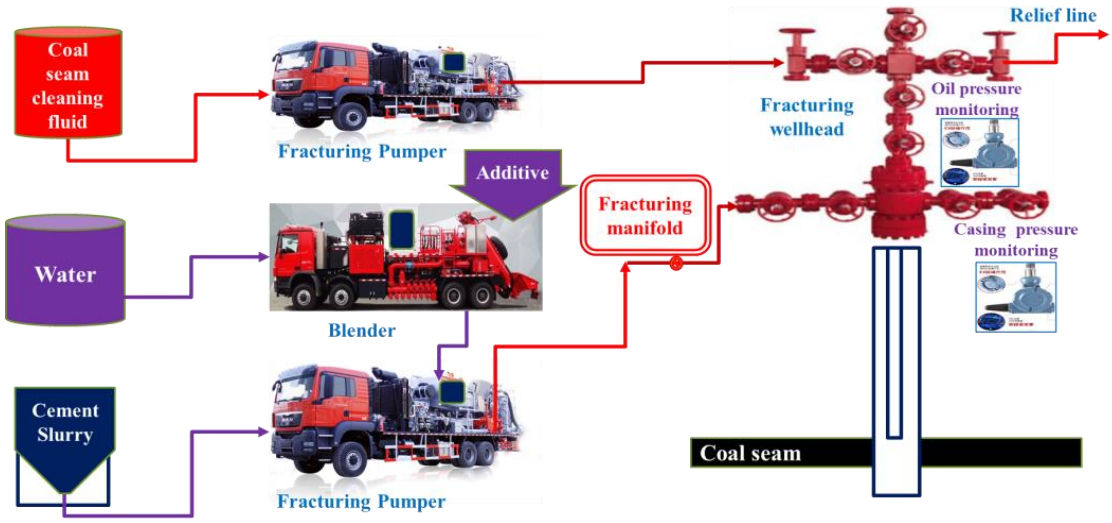

Figure 19. On-site fracturing operation flow chart.

4.3. Fracturing Operation Curve

Figure 20 illustrates the fracturing operation curve of graphene–foam–cement slurry in April 2022. Analysis is as follows:

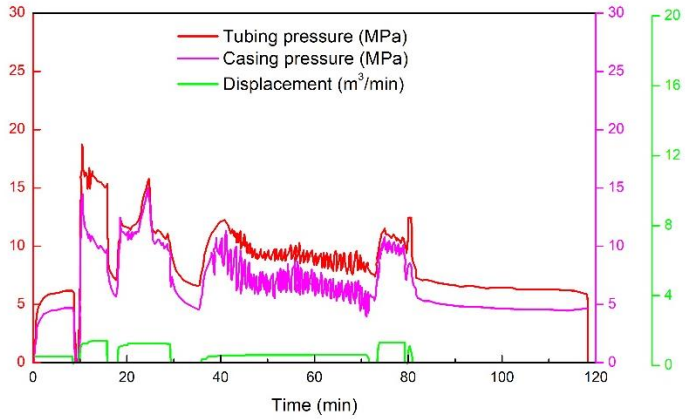

Figure 20. Fracturing operation curve of graphene–foam–cement slurry.

1. Coal seam cleaning fluid was injected into the formation through the oil pipe for 13 m^3 with a displacement of 1.3–1.5 m^3/min. The tubing pressure decreased from a maximum of 19 MPa to 16 MPa, and the casing pressure decreased from a maximum of 14 MPa to 9 MPa, indicating that the coal seam cleaning fluid entered the coal seam to improve the permeability.

2. Graphene–foam–cement slurry was injected into the formation through the casing for 13 m^3 with a displacement of 0.4–0.6 m^3/min. The tubing pressure dropped from 13 MPa to 8 MPa and the casing pressure dropped from 11 MPa to 7 MPa in the beginning stage. 1–2 MPa of high-frequency jumps in tubing pressure and casing pressure indicated that the coal seam had started fracturing. In the middle stage, the tubing pressure dropped from 9 MPa to 8 MPa, and the casing pressure dropped from 7 MPa to 6 MPa. 1–2 MPa of high-frequency jumps in tubing pressure and casing pressure indicated that the coal seam fracture extended normally. The graphene–foam–cement slurry continuously opened the end cuttings and face cuttings of the coal seam, forming a three-dimensional microfracture network of SRV.

3. Displacement fluid was injected into the wellbore from the casing for 6 m^3 and injected into the wellbore from the oil pipe for 1 m^3. The tubing pressure decreased from the maximum 13 MPa to 8 MPa, and the casing pressure decreased from the maximum 13 MPa to 8 MPa after stopping the pump.

4. The total prepared fluid volume was 45 m^3, and 33 m^3 was actually injected. 27 m^3 was injected into the formation after subtracting 6 m^3 in the wellbore. The small-scale SCGPCS fracturing with no sand addition, small fluid volume and small displacement was successfully tested for the first time on site.

4.4. Test Well Interpretation Data

IDSSL Freewheeling Well Test Analysis System

The basic theory of the software is to study the amount of change in the rate of the fluid in the same time. Rate tests are conducted for different lithologies, pore seepage patterns and fluid characteristics. A mathematical model of rate and reservoir characteristic parameters is established to find the interpretation and evaluation method of physical parameters of the reservoir. Table 1 shows the result of pressure drop interpretation test.

Table 1. Pressure drops interpretation test.

Pressure Drops Interpretation	Test Radius/m	Raw Permeability of Coal Seam/mD	Permeability of SCGPCS Fracturing/mD
Coal seam cleaning fluid pressure drop test	19.24	1.4	14.22
Dynamic fracturing crack pressure drop testing of graphene–foam–cement slurry fracturing	71.58	1.4	34,500
Static fracturing crack pressure drop testing of graphene–foam–cement slurry fracturing	56.95	1.4	57.1652

Figure 21 presents the pressure drop test of the coal seam cleaning fluid. The crack half-length of the coal seam treated with the coal seam cleaning fluid was 19.24 m. The average permeability of the treated coal seam was 14.22 mD. Figure 22 illustrates the dynamic fracturing crack pressure drop testing of graphene–foam–cement slurry fracturing. The fracturing crack half-length was 71.58 m. The average permeability in the fracturing crack was 34,500 mD. Figure 23 shows the static fracturing crack pressure drop testing after graphene–foam–cement slurry fracturing. The supported fracturing crack half-length was 56.95 m. The supported fracturing crack permeability near wellbore was 56.265 mD. This is in good agreement with the permeability of SCGPCS in the laboratory (57.24 mD). The unsupported fracturing crack permeability in crack tip was 4.29439 mD.

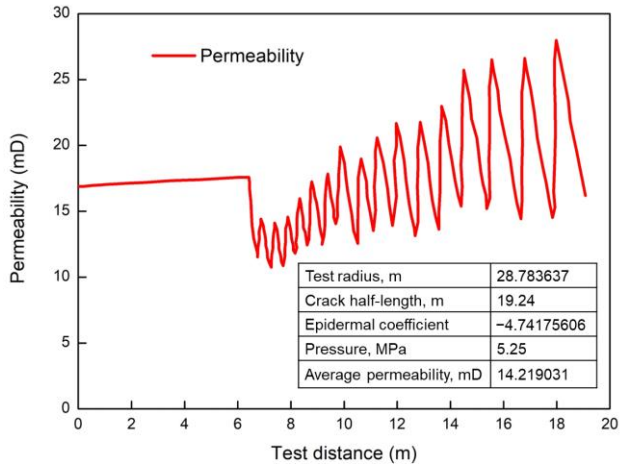

Figure 21. Coal seam cleaning fluid pressure drop test.

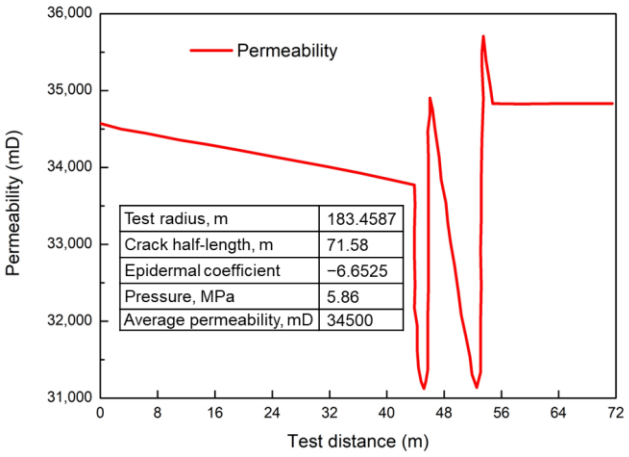

Figure 22. Dynamic fracturing crack pressure drop testing of graphene–foam–cement slurry fracturing.

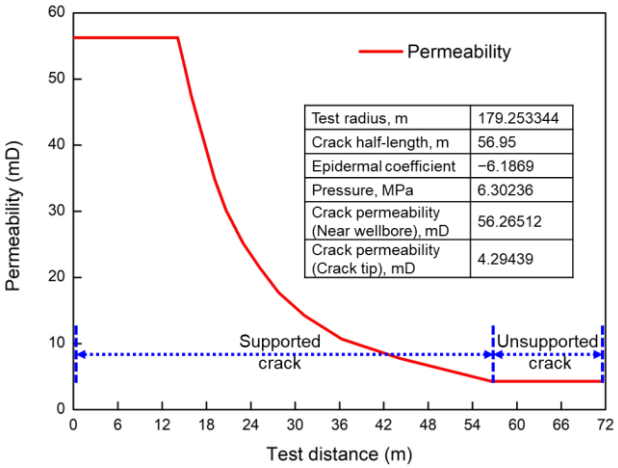

Figure 23. Static fracturing crack pressure drop testing after graphene–foam–cement slurry fracturing.

5. Possible Mechanisms

Figure 24 illustrates the possible mechanism of graphene–foam–cement slurry forming high permeability SCGPCS.

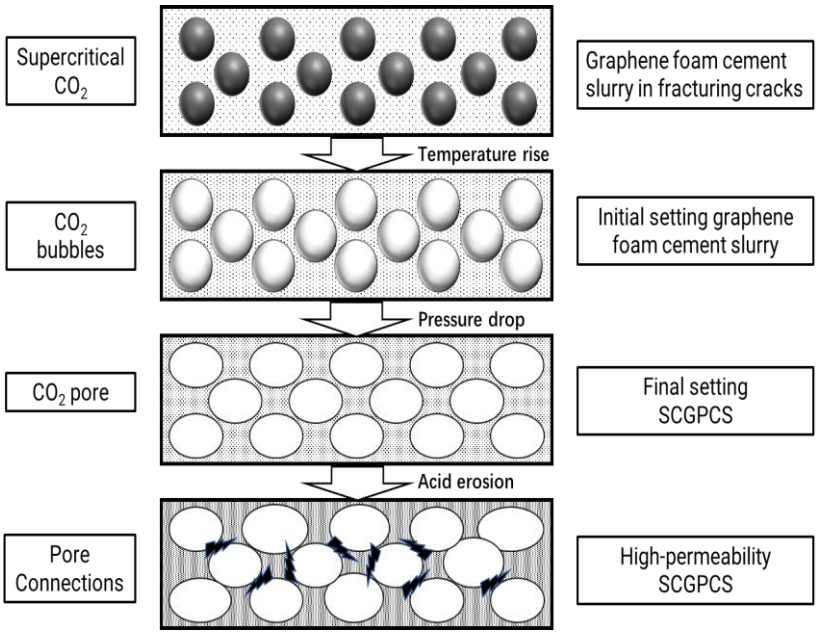

Figure 24. Mechanism diagram of graphene–foam–cement slurry forming high permeability SCGPCS.

1. Graphene–foam–cement slurry is mixed with gas-generating agents and other additives to inject into coal seam cracks and generate supercritical carbon dioxide.

2. Supercritical CO_2 is vaporized into small, compressed CO_2 bubbles with the heat exchange between the graphene–foam–cement slurry and the coal seam.

3. The exothermic hydration of the graphene–foam–cement slurry raises the internal temperature. The pressure inside the graphene–foam–cement slurry decreases by diffusion into the formation. The temperature rise and pressure drop inside the graphene–foam–cement slurry will result in larger supercritical CO_2 bubbles and bubble deformation, which will result in thinner bubble walls. The CO_2 inside the pore dissolves in the water inside the SCGPCS, forming a carbonic acid solution. The carbonic acid solution dissolves the bubble walls, connecting the formed pore structure and improving the permeability of the cement stone.

6. Conclusions

A new SCGPCS fracturing fluid system was investigated to be used in coalbed methane fracturing. The following conclusions were obtained.

1. The SCGPCS system uses sulphoaluminate cement, which can set quickly after entering the formation and reach large strength in a short period of time and can form an effective fracture support structure after fracturing.

2. GPG can be used as a foam stabilizer for SCGPCS system. Surfactant in GPG can be adsorbed on the gas/liquid interface to reduce the surface tension, thus playing a stabilizing role in foam. Graphene nanosheets in GPG can be adsorbed on the gas/liquid interface to form a liquid film with high mechanical strength, enhancing the stability of foam.

3. The graphene–foam–cement slurry system has better rheology, and it is easy to be pumped into the formation. Temperature rise, pressure drop, and carbonic acid dissolution will connect the formed pore structure and improve the permeability of the SCGPCS.

4. The small-scale SCGPCS fracturing with no sand addition, small fluid volume and small displacement was successfully tested for the first time in an extra-low desorption pressure coal seam, which laid the foundation for the next step of medium-scale fracturing test. It is hoped that the medium-scale fracturing test can be completed in November 2022 and promoted to the entire coalbed methane development industry.

Author Contributions: Conceptualization, D.L.; methodology, D.L. and P.L.; experiment design, D.L. and X.P.; experiment, D.L. and L.F.; data analysis, D.L. and G.X.; field validation, T.Z. and W.F.; writing—review and editing, D.L. and P.L.; funding acquisition, G.X. All authors have read and agreed to the published version of the manuscript.

Funding: This study was funded by the Science and Technology Cooperation Project of the CNPC-SWPU Innovation Alliance (Grant No. 2020 CX040102 and 2020 CX040201).

Data Availability Statement: Not applicable.

Conflicts of Interest: The authors declare no conflict of interest.

References

1. Hassanpouryouzband, A.; Joonaki, E.; Edlmann, K.; Haszeldine, R.S. Offshore geological storage of hydrogen: Is this our best option to achieve net-zero? *ACS Energy Lett.* **2021**, *6*, 2181–2186. [CrossRef]
2. Hassanpouryouzband, A.; Joonaki, E.; Vasheghani Farahani, M.; Takeya, S.; Ruppel, C.; Yang, J.; English, N.J.; Schicks, J.M.; Edlmann, K.; Mehrabian, H.; et al. Gas hydrates in sustainable chemistry. *Chem. Soc. Rev.* **2020**, *49*, 5225–5309.
3. Vasheghani Farahani, M.; Hassanpouryouzband, A.; Yang, J.; Tohidi, B. Development of a coupled geophysical–geothermal scheme for quantification of hydrates in gas hydrate-bearing permafrost sediments. *Phys. Chem. Chem. Phys.* **2021**, *23*, 24249–24264. [CrossRef] [PubMed]
4. Lu, Y.Y.; Zhang, H.D.; Zhou, Z.; Ge, Z.L.; Chen, C.J.; Hou, Y.D.; Ye, M.L. Current Status and Effective Suggestions for Efficient Exploitation of Coalbed Methane in China: A Review. *Energy Fuels* **2021**, *35*, 9102–9123. [CrossRef]
5. Tao, S.; Chen, S.; Pan, Z. Current Status, Challenges, and Policy Suggestions for Coalbed Methane Industry Development in China: A Review. *Energy Sci. Eng.* **2019**, *7*, 1059–1074. [CrossRef]
6. Qin, Y.; Moore, T.A.; Shen, J.; Yang, Z.; Shen, Y.; Wang, G. Resources and Geology of Coalbed Methane in China: A Review. *Int. Geol. Rev.* **2018**, *60*, 777–812. [CrossRef]
7. Colmenares, L.B.; Zoback, M.D. Hydraulic Fracturing and Wellbore Completion of Coalbed Methane Wells in the Powder River Basin, Wyoming: Implications for Water and Gas Production. *AAPG Bull.* **2007**, *91*, 51–67. [CrossRef]
8. Zhang, J. Numerical Simulation of Hydraulic Fracturing Coalbed Methane Reservoir. *Fuel* **2014**, *136*, 57–61. [CrossRef]
9. Xu, J.; Zhai, C.; Qin, L. Mechanism and Application of Pulse Hydraulic Fracturing in Improving Drainage of Coalbed Methane. *J. Nat. Gas Sci. Eng.* **2017**, *40*, 79–90. [CrossRef]
10. Fan, S.; Zhang, D.; Wen, H.; Cheng, X.; Liu, X.; Yu, Z.; Hu, B. Enhancing Coalbed Methane Recovery with Liquid CO_2 Fracturing in Underground Coal Mine: From Experiment to Field Application. *Fuel* **2021**, *290*, 119793. [CrossRef]
11. Huang, Q.; Liu, S.; Wang, G.; Wu, B.; Zhang, Y. Coalbed Methane Reservoir Stimulation Using Guar-based Fracturing Fluid: A Review. *J. Nat. Gas Sci. Eng.* **2019**, *66*, 107–125. [CrossRef]
12. Barati, R.; Liang, J.T. A Review of Fracturing Fluid Systems Used for Hydraulic Fracturing of Oil and Gas Wells. *J. Appl. Polym. Sci.* **2014**, *131*, 40735. [CrossRef]
13. Li, Q.; Xing, H.; Liu, J.; Liu, X. A Review on Hydraulic Fracturing of Unconventional Reservoir. *Petroleum* **2015**, *1*, 8–15. [CrossRef]
14. Van Voast, W.A. Geochemical Signature of Formation Waters Associated with Coalbed Methane. *AAPG Bull.* **2003**, *87*, 667–676. [CrossRef]
15. Pan, Z.; Connell, L.D.; Camilleri, M. Laboratory Characterization of Coal Reservoir Permeability for Primary and Enhanced Coalbed Methane Recovery. *Int. J. Coal Geol.* **2010**, *82*, 252–261. [CrossRef]
16. Gash, B.W. Measurement of "Rock Properties" in Coal for Coalbed Methane Production. Presented at the Annual Technical Conference and Exhibition, Dallas, TX, USA, 6–9 October 1991; pp. 221–230.
17. Chen, Y.; Liu, D.; Yao, Y.; Cai, Y.; Chen, L. Dynamic Permeability Change During Coalbed Methane Production and Its Controlling Factors. *J. Nat. Gas Sci. Eng.* **2015**, *25*, 335–346. [CrossRef]
18. Park, S.Y.; Liang, Y. Biogenic Methane Production from Coal: A Review on Recent Research and Development on Microbially Enhanced Coalbed Methane (MECBM). *Fuel* **2016**, *166*, 258–267. [CrossRef]
19. Yang, S.; Wu, X.; Han, L.; Wang, J.; Feng, Y. Migration of Variable Density Proppant Particles in Hydraulic Fracture in Coal-bed Methane Reservoir. *J. Nat. Gas Sci. Eng.* **2016**, *36*, 662–668. [CrossRef]
20. Keshavarz, A.; Badalyan, A.; Johnson, R.; Bedrikovetsky, P. Productivity Enhancement by Stimulation of Natural Fractures Around a Hydraulic Fracture Using Micro-sized Proppant Placement. *J. Nat. Gas Sci. Eng.* **2016**, *33*, 1010–1024. [CrossRef]
21. Li, H.; Huang, B.; Cheng, Q.; Zhao, X. Optimization of Proppant Parameters for CBM Extraction Using Hydrofracturing by Orthogonal Experimental Process. *J. Geophys. Eng.* **2020**, *17*, 493–505. [CrossRef]
22. Al-Muntasheri, G.A. A Critical Review of Hydraulic-fracturing Fluids for Moderate- to Ultralow-Permeability Formations over the Last Decade. *SPE Prod. Oper.* **2014**, *29*, 243–260. [CrossRef]
23. Warner, N.R.; Darrah, T.H.; Jackson, R.B.; Millot, R.; Kloppmann, W.; Vengosh, A. New Tracers Identify Hydraulic Fracturing Fluids and Accidental Releases from Oil and Gas Operations. *Environ. Sci. Technol.* **2014**, *48*, 12552–12560. [CrossRef] [PubMed]
24. Zhang, A.; Cao, D.; Wei, Y.; Rufford, T.E. Characterization of fines produced during drainage of coalbed methane reservoirs in the Linfen block, Ordos Basin. *Energy Explor. Exploit.* **2020**, *38*, 1664–1679. [CrossRef]

25. Han, G.; Ling, K.; Wu, H.; Gao, F.; Zhu, F.; Zhang, M. An Experimental Study of Coal-fines Migration in Coalbed-methane Production Wells. *J. Nat. Gas Sci. Eng.* **2015**, *26*, 1542–1548. [CrossRef]
26. Gao, D.; Liu, Y.; Wang, T.; Wang, D. Experimental Investigation of the Impact of Coal Fines Migration on Coal Core Water Flooding. *Sustainability* **2018**, *10*, 4102. [CrossRef]
27. Chang, F.F.; Berger, P.D.; Lee, C.H. In-situ Formation of Proppant and Highly Permeability Blocks for Hydraulic Fracturing. Presented at the SPE Hydraulic Fracturing Technology Conference, The Woodlands, TX, USA, 3–5 February 2015. Paper SPE-173328-MS.
28. Liang, F.; Sayed, M.; Al-muntasheri, G.A.; Chang, F.F.; Li, L. A comprehensive review on proppant technologies. *Petroleum* **2016**, *2*, 26–39. [CrossRef]
29. Stovall, T.; De Larrard, F.; Buil, M. Linear Packing Density Model of Grain Mixtures. *Powder Technol.* **1986**, *48*, 1–12. [CrossRef]
30. Frigione, G.; Marra, S. Relationship Between Particle Size Distribution and Compressive Strength in Portland Cement. *Part Size Distrib.* **1976**, *6*, 113–127. [CrossRef]
31. Li, S.; Li, Z.; Wang, P. Experimental Study of the Stabilization of CO_2 Foam by Sodium Dodecyl Sulfate and Hydrophobic Nanoparticles. *Ind. Eng. Chem. Res.* **2016**, *55*, 1243–1253. [CrossRef]
32. Chang, S.H.; Grigg, R.B. Effects of Foam Quality and Flow Rate on CO_2-foam Behavior at Reservoir Temperature and Pressure. *SPE Reserv. Eval. Eng.* **1999**, *2*, 248–254. [CrossRef]
33. Mo, D.; Yu, J.; Liu, N.; Lee, R. Study of the Effect of Different Factors on Nanoparticle-Stablized CO_2 Foam for Mobility Control. In Proceedings of the SPE Annual Technical Conference and Exhibition, San Antonio, TX, USA, 8–10 October 2012.
34. Telesca, A.; Marroccoli, M.; Pace, M.L.; Tomasulo, M.; Valenti, G.L.; Monteiro, P.J.M. A Hydration Study of Various Calcium Sulfoaluminate Cements. *Cem. Concr. Compos.* **2014**, *53*, 224–232. [CrossRef]
35. Zhang, L.; Glasser, F.P. Hydration of Calcium Sulfoaluminate Cement at Less than 24 h. *Adv. Cem. Res.* **2002**, *14*, 141–155. [CrossRef]
36. Borštnar, M.; Daneu, N.; Dolenec, S. Phase Development and Hydration Kinetics of Belite-calcium Sulfoaluminate Cements at Different Curing Temperatures. *Ceram. Int.* **2020**, *46*, 29421–29428. [CrossRef]
37. Satava, V.; Veprek, O. Thermal Decomposition of Ettringite Under Hydrothermal Conditions. *J. Am. Ceram. Soc.* **1975**, *58*, 357–359. [CrossRef]
38. Barnes, P. Thermal decomposition of ettringite $Ca_6[Al(OH)_6]_2(SO_4)_3$ $26H_2O$. *J. Chem. Soc. Faraday Trans.* **1996**, *92*, 2125–2129.
39. Li, L.; Wang, R.; Zhang, S. Effect of Curing Temperature and Relative Humidity on the Hydrates and Porosity of Calcium Sulfoaluminate Cement. *Constr. Build. Mater.* **2019**, *213*, 627–636. [CrossRef]
40. Kaufmann, J.; Winnefeld, F.; Lothenbach, B. Stability of Ettringite in CSA Cement at Elevated Temperatures. *Adv. Cem. Res.* **2016**, *28*, 251–261. [CrossRef]
41. Deschner, F.; Lothenbach, B.; Winnefeld, F.; Neubauer, J. Effect of Temperature on the Hydration of Portland Cement Blended with Siliceous Fly Ash. *Cem. Concr. Res.* **2013**, *52*, 169–181. [CrossRef]
42. Rastrup, E. Heat of Hydration in Concrete. *Mag. Concr. Res.* **1954**, *6*, 79–92. [CrossRef]
43. Chen, M.C.; Wang, K.; Xie, L. Deterioration Mechanism of Cementitious Materials under Acid Rain Attack. *Eng. Fail. Anal.* **2013**, *27*, 272–285. [CrossRef]
44. Pastore, T.; Cabrini, M.; Coppola, L.; Lorenzi, S.; Marcassoli, P.; Buoso, A. Evaluation of the Corrosion Inhibition of Salts of Organic Acids in Alkaline Solutions and Chloride Contaminated Concrete: Organic Inhibitors for Chloride Contaminated Concrete. *Mater. Corros.* **2011**, *62*, 187–195. [CrossRef]